





Enhancing Echo Processing Through the Integration of Support Vector Machine and Weber's Law Descriptors

Mehdia Hedir¹^a, Fethi Demim²^b, Ali Zakaria Messaoui³^c, Aimen Abdelhak Messaoui³^d,
Hadjira Belaidi⁴^e, Abdenebi Rouigueb⁵^f and Abdelkrim Nemra²^g

¹Faculty of Technology of M'Hamed BOUGARA University-Boumerdes (UMBB), Algeria

²Laboratory of Guidance and Navigation, Ecole Militaire Polytechnique, Bordj El Bahri, Algiers, Algeria

³Laboratory of Complex Systems Control and Simulators, Ecole Militaire Polytechnique, Bordj El Bahri, Algiers, Algeria

⁴Signals and Systems Laboratory, Institute of Electrical and Electronic Engineering, University M'Hamed Bougara of Boumerdes, Algeria

⁵Laboratory of Artificial Intelligence and Virtual Reality, Ecole Militaire Polytechnique, Bordj El Bahri, Algiers, Algeria

Keywords: Cloud, Tracking, Ground Echoes, SVM, WLD, WLBP.

Abstract: Removing ground echoes from weather radar images is a topic of great importance due to their significant impact on the accuracy of processed data. To address this challenge, we aim to develop methods that effectively eliminate ground echoes while preserving the precipitation, which is a crucial meteorological parameter. To accomplish this, we propose to test Local Descriptors based on Weber's law (WLD), as well as descriptors that combine Weber's law with Local Binary Pattern (WLBP), using Support Vector Machine (SVM) classifiers to automate the recognition of both types of echoes. The proposed methods are rigorously tested at the sites of Setif and Bordeaux to evaluate their effectiveness in accurately identifying the ground echoes and precipitation. The results of our experiments demonstrate that the proposed techniques are highly effective in eliminating ground echoes while preserving the precipitation, and can be considered satisfactory for practical applications in meteorological data processing.


1 INTRODUCTION


The scientific community is compelled to proactively address the complexities of the atmosphere and its intricate energy exchanges. Weather radar, a pivotal tool for national weather services, airports, and meteorological research departments, is employed to monitor precipitation, necessitating the implementation of various filtering methods to eliminate false echoes. Numerous studies have concentrated on refining radar data filtering techniques within this domain.


In a seminal work, the authors of (Paixao et al., 2015) devised a method specifically tailored for iden-


tifying areas of severe precipitation. Big data techniques and technologies were proposed in (Fathi et al., 2022) to effectively manage and analyze vast amounts of meteorological data. Beyond its conventional applications, weather information has found relevance in medical studies, exemplified by research on virus spread, such as COVID-19 (Malki et al., 2020). Nevertheless, meteorological data faces contamination challenges from unwanted echoes, including Anomalous Propagation (APs) and ground echoes (Kaissasou et al., 2015). AP occurrences, associated with temperature inversions and high humidity gradients, were modeled using Markov chains in ((Haddad et al., 2000)). Textural features were effectively employed in (Haddad et al., 2004) to mitigate APs and soil echoes, while fuzzy logic strategies were explored in (Cho et al., 2006), (Islam et al., 2012).


In preceding research, a combination of textural characteristics derived from co-occurrence matrices, Support Vector Machines (SVM), and Convolutional Neural Networks (CNN) were leveraged to dis-


^a <https://orcid.org/0000-0002-9089-8007>


^b <https://orcid.org/0000-0003-0687-0800>

^c <https://orcid.org/0000-0001-5753-5776>

^d <https://orcid.org/0000-0003-0687-0800>

^e <https://orcid.org/0000-0003-2424-626X>

^f <https://orcid.org/0000-0001-6530-2160>

^g <https://orcid.org/0000-0001-9237-9449>

tinguish precipitation echoes from background noise (Hedir and Haddad, 2016). Additionally, local binary models and their variations were investigated for eliminating unwanted echoes (Hedir et al., 2018), (Hedir et al., 2019).

In this study, we extend the descriptor repertoire for echo characterization to incorporate Weber's Law Descriptor (WLD) (Chen et al., 2010) and Weber's Local Binary Model (WLB) (Liu et al., 2013), (Cortes and Vapnik, 1995). These features serve as inputs to develop a robust SVM classifier (Cervantes et al., 2020), (Rouigeb et al., 2022), (Rouigeb et al., 2023), capable of discerning various types of echoes.

The organization of this work unfolds as follows: Section II details the descriptors utilized in this study, while Section III focuses on the Support Vector Machine classifier. Section IV provides insights into the databases used for validating the proposed approach and presents the obtained results. Lastly, Section V offers concluding remarks and outlines potential future directions.

2 LOCAL DESCRIPTORS

2.1 Local Binary Pattern

A proposed descriptor to characterize a local region is part of the Local Binary Pattern (LBP) approach described in (Ojala et al., 2002). LBP works by computing a binary code for each 3×3 neighborhood by dividing the values of the central pixel value (g_c) by the eight neighbors (g_p), where the value 1 is assigned for a positive outcome and the value 0 for a negative result (see Eq. (1)). This standard basis of LBP produces 256 texture patterns. A result is a binary number that represents the LBP code. The calculation of the aforementioned code is illustrated in Figure 1. This figure not only demonstrates the computational process but also provides visual clarity to the methodology discussed.

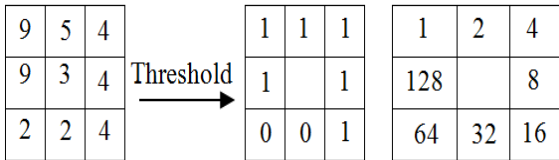


Figure 1: Calculation of the LBP code.

$$LBP_{P,R} = \sum_{i=0}^{P-1} (g_i - g_c)2^i = 159 \text{ with } \begin{cases} 1, & x \geq 0 \\ 0, & x < 0 \end{cases} \quad (1)$$

where g_c is the central pixel and g_i are the neighbors. The 3×3 neighborhood size of LBP prevents it from tracking large constructions. The operators are expanded to encompass neighborhoods of various sizes to address this issue. The LBP calculation can be applied to a symmetric circular neighborhood with radius R and P expressing the number of evenly spaced samples. The following equations can be used to determine the coordinates of g_p .

$$\begin{cases} g_x = x_c + \cos\left(\frac{2\pi p}{P}\right) \\ g_y = y_c - \sin\left(\frac{2\pi p}{P}\right) \end{cases} \quad (2)$$

In image processing, interpolation is used to establish the gray level of a neighbor's coordinates that are not always found in the center of a pixel. The multiscale Local Binary Pattern (LBP) was developed based on this concept, and to enhance its characterization, two more ideas are included: uniformity and non-uniformity. The uniform binary pattern incorporates a maximum of two transitions from 1 to 0 and vice versa, while non-uniform patterns have more than two transitions. The $LBP_{P,R}^{\mu 2}$ operator is calculated using these concepts. This information is found in (Ojala et al., 2002).

$$LBP_{P,R}^{\mu 2}(x,y) = \begin{cases} I(LBP_{P,R}^{\mu 2}(x,y)) \text{ if } U(LBP_{P,R}) \\ \leq 2, I(Z) \in [0, (P-1)P+1] \\ (P-1)P+2 \quad \text{Otherwise} \end{cases} \quad (3)$$

The circular symmetry of the neighborhood facilitates the definition of a secondary pattern, $LBP_{P,R}^i$, which remains invariant not only to monotonic transformations of the gray level scale but also to rotations of the image. This second pattern, known as the rotation-invariant LBP, is derived as follows:

$$LBP_{P,R}^i = \min\{ROR(LBP_{P,R}(x,y), i) / i \in [0, P-1]\} \quad (4)$$

We conduct a thorough investigation by testing different combinations of radius and the number of neighbors to determine the optimal parameter values for the Local Descriptors and the Local Binary Pattern descriptors used in our proposed methods. The value $ROR(a, i)$ corresponds to the result of i successive circular shifts to the right of the bits of number a (coded on P bits).

2.2 Weber Law Descriptor

The relationship between a mental sensation and the physical size of a stimulus is described by Weber's law. The principle was initially observed by the German physiologist E.H. Weber and finds application across different stimuli, including the correlation between the perceived intensity of a sound and the associated pressure wave. The modern technique involves

two components, the excitation difference and the orientation gradient, and is considered a robust descriptor. Weber's law is expressed as $\Delta I/I = K$, where ΔI is the threshold increment and I is the initial stimulus intensity. Reference (Chen et al., 2010) is cited as the source of Weber's law.

Differential Excitation

This component is noted by $\xi(x_c)$ with x_c the current pixel, its intensity must be different from zero. It is modeled by the arc tangent of the sum of the differences of intensities between the current pixel and its neighbors divided by the intensity of the current pixel as it is represented by Eq. (5):

$$\xi(x_c) = \arctan\left(\frac{\sum_{i=0}^{P-1}(x_i - x_c)}{x_c}\right) \quad (5)$$

with x_i represents the i^{th} neighboring pixel of the current pixel, and the value of $\xi(x_c)$ lies within the range of $[-\frac{\pi}{2}, \frac{\pi}{2}]$. When $\xi(x_c)$ is positive, it indicates that the neighborhood is darker than the current pixel.

Orientation

The ratio between the change in the horizontal direction and the vertical direction of an image is used to calculate the orientation gradient. Figure 3 offers a summary of the calculation's specifics. These mathematical equations can be used to represent this calculation as can be seen in Eq. (6), where $v_{10} = x_5 - x_1$, $v_{11} = x_7 - x_3$ and x_1, x_3, x_5 and x_7 are the neighbors of pixel x_c on 3×3 neighborhood as shown in Fig. 2.

$$\theta = \arctan\left(\frac{v_{10}}{v_{11}}\right) \quad (6)$$

x_0	x_1	x_2
x_7	x_c	x_3
x_6	x_5	x_4

Figure 2: Demonstration of 3×3 neighborhood.

Weber Local Binary Pattern Descriptor

Since LBP can extract more information than the orientation gradient, it was chosen as a part of the Weber descriptor. The Local Binary Pattern Descriptor (LBP) is a robust descriptor that has been used in many applications. The LBP vector is computed by

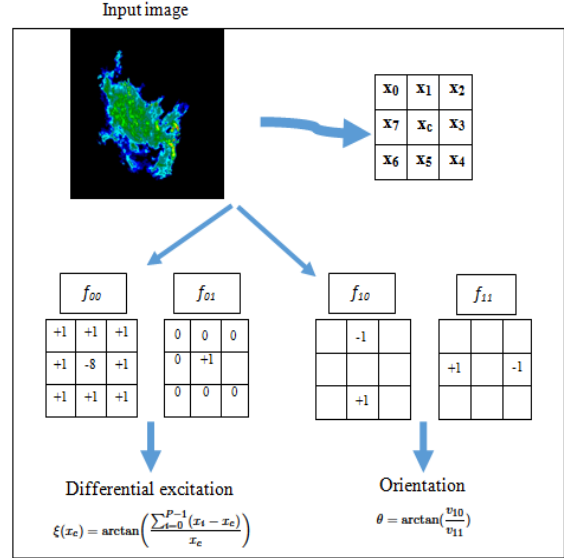


Figure 3: Example of gradient calculation based on excitation for an image (Chen et al., 2010).

taking into account the eight adjacent pixels, making it a discriminating descriptor. However, the orientation gradient, which only considers four pixels, preserves more information about the local structure. The uniform LBP is preferred due to the prevalence of uniform patterns, as shown in previous experiments. The formula for calculating WLBP for an image $f(x, y)$ at position (x, y) is also provided.

$$g(x, y) = h(x, y) \otimes f(x, y) \quad (7)$$

$$h(x, y) = \exp\left(-\frac{x^2 + y^2}{2\sigma^2}\right) \quad (8)$$

where $h(x, y)$ is the 2D Gaussian function and $g(x, y)$ is the convolution product of $h(x, y)$ and $f(x, y)$. Subsequently, the estimation of ΔI is done by equation:

$$\Delta I = \nabla^2[h(x, y) \otimes f(x, y)] = \frac{1}{\pi\sigma^4} \left(\frac{x^2 + y^2}{2\sigma^2} - 1 \right) \exp\left(-\frac{1}{2\sigma^2}(x^2 + y^2)\right) \quad (9)$$

In the case of the differential excitation, it is presented by $\xi(x_c) = \arctan(\Delta I/I)$, where I refers to the current pixel x_c 's gray level intensity. Theoretically, WLBP ought to be more discriminating than LBP; however, this is really due to the interaction between LBP and the excitation difference, which contributes significantly to the information. The WLBP is more illuminating and strong while yet maintaining the discrimination.

3 SUPPORT VECTOR MACHINE

The Support Vector Machine (SVM) concept's central principle is the learning-based classification or recognition of data. The latter generates an output $y = f(x)$ from a set of inputs x_i . The goal is to determine a function f from the observation of numerous input/output pairs (also known as training data), where x_i represents any item and y_i represents a class label. This function, which corresponds to model (Cervantes et al., 2020), effectively categorizes each input/output pair into its respective class with precision. The task is to find a decision boundary that separates the space into two regions. Finding a decision boundary that divides the space into two sections is the problem at hand. The data is typically not linearly separable, so a kernel function is utilized to increase the distance between them. The data is represented in a different place called feature space. The SVM training tool utilizes the LIBSVM library. Each sample was split into two major groups (training and testing). We employ the Radial Basis Function (RBF) kernel for processing, which is presented as follows:

$$k(x_i, x_j) = \exp(-\gamma \|x_i - x_j\|^2), \quad \gamma > 0 \quad (10)$$

γ acts as a parameter that determines the hyperplane during model training, with x_i representing a sample of input data and x_j denoting all other samples. Consequently, the decision function can be formulated as:

$$f(x) = \sum_{i=1}^S \alpha_i y_i k(x, x_i) + b \quad (11)$$

α_i denotes the Lagrange multipliers with values ranging between 0 and C , where b stands for the bias, and C represents a positive constant that regulates errors and maximizes the margin.

4 DATABASE AND METHODOLOGY BASED APPROACH

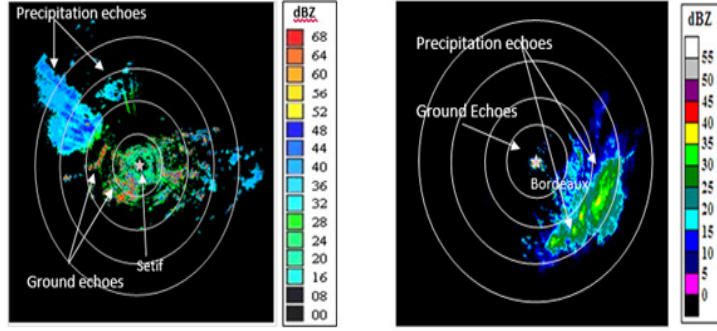
The 5799 photos acquired in Setif in 1999 and the 10.052 photographs taken in Bordeaux in 1996 make up the database used for this study. Two incoherent pulsed radars captured the 512×512 pixel images with a resolution of 1 km per pixel, which were then displayed using the Plan Position Indicator Mode (PPIM). Bordeaux has a gray level coding of 64 and Setif has a gray level of 16. The first radar is situated close to Setif at the summit of Meghres Mountain. The geography of the province of Setif is divided into several regions: in the north, the Babors

Chain rises to a height of 2004 m. The Djurdjura and Bibans Mountains, with peak elevations of 2300 m and 1417 m, are located in the southwest. The altitude at the region's center ranges from 800 to 1300 m. Every 15 minute, photos of Setif were captured as shown in Fig. 4(a). The Bordeaux radar, which is situated at Bordeaux MÃ©rignac Airport, is a member of the Meteo-France-run operational French weather radar network. The Pyrenees Mountains, which rise to a height of 3000 m in the south and are located 200 km from the radar, as well as the industrial sector that surrounds the radar, are only two of the challenges in the Bordeaux region. The main reason for permanent echoes in this area is the industrial area. Every day, five minutes were spent gathering these photographs. Fig. 4(b) displays an illustration from the Bordeaux website. Initially, a database comprising two sets of images is compiled. One set exclusively portrays precipitation echoes, selected from images where distinguishing between ground echoes and precipitation is straightforward. The other set comprises images captured during clear weather conditions, devoid of precipitation, depicting solely ground echoes. In the classification process, training data for precipitation is assigned the label (-1), while training data for ground echoes is labeled (1).

The model design involves two key processes: learning and validation. The training data is partitioned into two segments, one for model training and the other for validating the optimal model. Subsequently, a separate set of labeled test data, previously unseen during the learning phase, is employed to evaluate the classifier's robustness. The allocation of pixels for training and testing at both Setif and Bordeaux sites is detailed in Table 1.

The SVM will be trained using the characteristic vectors to identify the ideal parameters (γ, η) . One of these vectors is used to learn and create SVM models, and the other is utilized to validate just one model out of the designed ones. With the introduction of the nonlinear kernel, nonlinear data is taken into account. The selection of a suitable kernel function and the modifying of its parameters form the foundation of nonlinear SVM design. We use the Radial Basis Function kernel in our strategy. This final example displays positive test findings. We can assess the effectiveness of the suggested strategy using the statistics in Table 2, where a and d represent the correct identification of precipitations and ground echoes, while b and c represent the false identification in order.

For better visualization of the WLD vector parameters, we propose to design a new descriptor which combines WLD's component and $LBP_{8,1}^{U^2}$. The LBP



(a) Image from Setif site. (b) Image from Bordeaux site.

Figure 4: Example of images from Setif and Bordeaux sites.

Table 1: Number of pixels used in training and testing for both databases.

Sites	Training data		Test data	
	Precipitations	Ground echoes	Precipitations	Ground echoes
Setif	6500	6500	88015	72590
Bordeaux	6500	6500	1378267	956738

consider the nine neighbors, the threshold lets the LBP be more sensitive to small gray level variation. This leads the descriptor to extract a maximum of local structure and it is very discriminating. However, WLD can perfectly extract the edges even in the presence of intense noise, this encourages us to use the WLD-LBP combination. We observed during experiments on the database that the uniform binary motif gives a percentage equal to 86% for images containing precipitations and 80% for those with ground echoes using $R = 1$ and $P = 8$, while for $R = 2$ and $P = 16$, the percentage is 67% for precipitation and 60% for ground echoes. We can note that the majority of the binary patterns are uniform, that's why we favored the $LBP_{8,1}^{U2}$.

4.1 Setif's Results

We consider two situations for the Setif site : the first concerns the case where we distinguish ground echoes from precipitations; the second describes the situation where the precipitation is covered by clutter. The results obtained in the first case are summarized in Table 3. The use of LBP^{ri} , LBP^{u2} and LBP^{riu2} shows an average efficiency in the treatment of echoes. Indeed, more than 79.6% of echoes are eliminated while the preservation of precipitation does not exceed 64%. Considering PODE for WLD, WLP and WLD-LBP, we notice that the second and third cases exhibit a good suppression of undesirable echoes with more than 92%, while WLD suppressed only 84.69%. However, the percentage of correct identification reaches its best score 90.13% with the

WLD-LBP descriptor as well as the SR which defines the positive identification of ground echoes among all the identifications with a rate equal to 94.93%. This shows that the information added in the modified WLD-LBP descriptor provided additional information for the identification of echoes. Fig. 5 shows the obtained results when we filter an image of Fig. 5(a) with LBP^{u2} and Fig. 5(b) with $D - LBP$. The second case is when the precipitations are covered by ground echoes, the estimations of statistical parameters are difficult so only visual appreciation is possible. Fig. 6 and Fig. 7 illustrate this situation, and the results are the same as for the first case.

4.2 Bordeaux's Results

The LBP variants exhibit a commendable rate of ground echo elimination, with the highest score achieved at 97.85% by LBP^{riu2} , while PODP does not exceed 75.89%. CIA remains acceptable across all three variants, with the best score reaching 76.77%. With WLP and WLD-LBP, PODE stands at 92.08% and 91.84% respectively, and PODP ranges between 80% and 82%. This highlights the effectiveness of our proposed descriptor in preserving precipitation while eliminating ground echoes.

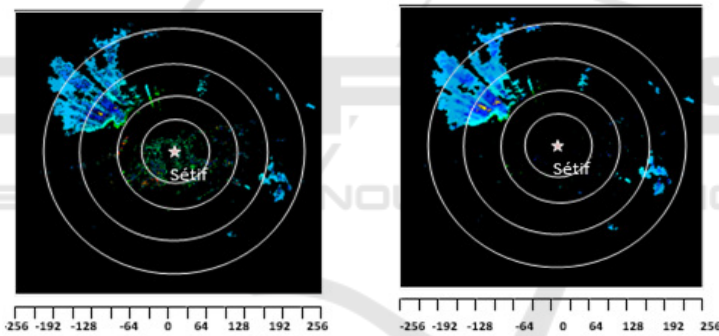
Notably, the ratio of parameter b to $c + d$ is considerably higher, owing to the greater number of precipitation pixels compared to ground echoes. Misclassification of 1% of precipitation echoes corresponds to 13782 pixels, representing 15% of ground echoes, significantly impacting the SR and CSI . FARE varies within the range of (73 – 84%), which is compara-

Table 2: Statistical parameters.

POD (Echoes)	POD (Precipitations)	FAR (Echoes)	FAR(Precipitations)
$PODE = \frac{d}{c+d}$	$PODP = \frac{a}{a+b}$	$FARE = \frac{b}{b+d}$	$FARP = \frac{c}{c+a}$
Success Ratio	Critical Success Index	Correct Identification Accuracy	/
$SR = \frac{d}{b+d}$	$CSI = \frac{a}{a+b+c}$	$CIA = \frac{a+d}{a+b+c+d}$	/

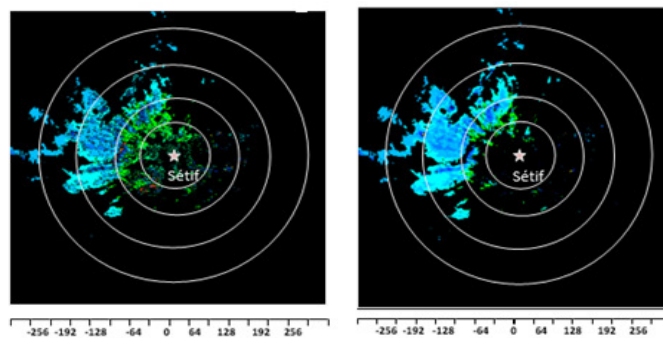
Table 3: Number of pixels used in training and testing for Setif databases.

Combination category		PODE	PODP	FARE	FARP	SR	CSI	CIA
LBP^{U2}	R1	83.74	62.48	35.19	17.66	64.80	57.56	72.09
LBP^{U2}	R2	77.85	16.36	56.56	52.73	43.43	38.65	44.16
LBP^{U2}	R3	85.56	11.79	55.55	50.23	44.44	41.34	45.13
LBP^{ri}	R1	85.52	56.52	38.13	17.43	61.86	56.00	69.63
LBP^{ri}	R2	67.81	57.18	43.36	31.70	56.63	44.63	61.98
LBP^{ri}	R3	61.41	63.65	41.78	33.33	58.21	42.62	62.63
LBP^{riu2}	R1	79.60	63.45	35.76	20.95	64.23	55.15	70.75
LBP^{riu2}	R2	81.64	53.34	40.92	22.10	59.07	52.14	66.13
LBP^{riu2}	R3	72.66	65.69	45.54	19.017	54.45	45.19	68.21
WLD		84.69	94.15	7.71	11.82	92.28	79.09	89.88
WLBP		92.51	76.34	23.66	7.48	76.33	71.89	83.65
WLD-LBP		92.51	80.97	5.06	26.26	94.93	88.15	90.13



(a) Filtered image with LBP^{u2} . (b) Case of separated echos image $D-LBP$.

Figure 5: Example of filtered images.



(a) Filtered image with LBP^{u2} . (b) Filtered image with $WLD-LBP$.

Figure 6: Example of two combination categories.

Table 4: Number of pixels used in training and testing for Bordeaux databases.

Combination category		PODE	PODP	FARE	FARP	SR	CSI	CIA
LBP^{U2}	R1	91.39	66.42	84.55	0.86	15.44	15.22	67.99
LBP^{U2}	R2	93.23	48.57	89.70	0.87	10.29	10.21	51.23
LBP^{U2}	R3	96.42	41.75	90.04	0.56	9.95	9.92	45.17
LBP^{ri}	R1	89.73	75.89	79.77	0.91	20.22	19.76	76.77
LBP^{ri}	R2	93.29	62.79	85.64	0.70	14.35	14.20	64.70
LBP^{ri}	R3	70.85	56.9	90.08	3.30	9.9	9.5	57.81
LBP^{riu2}	R1	89.54	69.08	83.78	1.00	16.21	15.91	70.36
LBP^{riu2}	R2	95.60	49.39	88.78	0.59	11.21	11.15	52.28
LBP^{riu2}	R3	97.85	44.13	90.14	0.30	9.85	9.83	47.29
WLD		88.45	80.17	76.02	1.00	23.97	23.24	80.72
WLBP		92.08	66.07	84.64	0.79	15.35	15.15	67.70
WLD-LBP		91.84	82.76	73.74	0.65	26.25	25.66	83.33

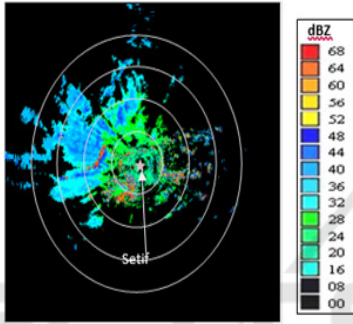


Figure 7: Image with ground echoes cover precipitations.

tively high due to the extensive surface area of precipitations.

As for the reflectivity-SVM method, our experiments yield the following performance metrics: PODE: 97.81%, FARE: 19.81%, SR: 80.19%, CSI: 78.78%, and CIA: 88.40%. Conversely, the reflectivity-NN method produces the following results: PODE: 88.40%, FARE: 19.81%, SR: 80.19%, CSI: 78.78%, and CIA: 88.4%, consistent with findings reported in (Ojala et al., 2002).

Importantly, our approach demonstrates superior suppression of ground echoes compared to the reflectivity-NN approach. Furthermore, our proposed methods utilizing WLD and WLD-LBP, when evaluated at the Setif site, outperform the techniques introduced in (Islam et al., 2012).

5 CONCLUSION

In this study, we initiated on an exploration of various descriptors aimed at effectively characterizing radar echoes. Among these descriptors, we investigated the Weber Law Descriptor (WLD), Local Binary Pat-

tern (LBP), and Weber-LBP (WLBP). The WLD furnishes a comprehensive representation of each 3×3 region by capturing its excitation difference and orientation components. Simultaneously, the LBP and WLBP furnish complementary insights across different scales, thereby enriching the descriptive power of our approach.

By combining the strengths of these descriptors, we developed the WLD-LBP method, employed for training Support Vector Machine (SVM) classifiers. These classifiers were assigned the task of distinguishing between different types of radar echoes. While our preliminary findings are promising, there is still significant scope for improvement. This could entail meticulous parameter tuning during training or exploring alternative descriptors that may better capture the unique characteristics of our data.

Our research provides valuable insights into the advancement of robust techniques aimed at filtering out ground echoes from weather radar images while preserving vital precipitation information. This undertaking represents a noteworthy stride towards improving the precision and dependability of radar data analysis in meteorological contexts. Moving forward, our future work will focus on addressing challenges such as optimizing the fusion of descriptors, enhancing the adaptability of classifiers to diverse weather conditions, and exploring innovative methods for handling complex radar data scenarios.

REFERENCES

- Cervantes, J., Garcia-Lamont, F., Rodriguez-Mazahua, L., and Lopez, A. (2020). A comprehensive survey on support vector machine classification: Applications, challenges and trends. pages 6189–215.
- Chen, J., Shan, S., He, C., Zhao, G., Pietikainen, M., Chen,

- X., and Gao, W. (2010). Wld: A robust local image descriptor. In *IEEE Transactions on Pattern Analysis and Machine Intelligence*, pages 1705–1720.
- Cho, Y., Lee, G., Kim, K., and Zawadzki, I. (2006). Identification and removal of ground echoes and anomalous propagation using the characteristics of radar echoes. pages 1206–1222.
- Cortes, C. and Vapnik, V. (1995). Support-vector networks. pages 273–297.
- Fathi, M., Kashani, M., Jameii, S., and Mahdipour, E. (2022). Big data analytics in weather forecasting: A systematic review. pages 1247–1275.
- Haddad, B., Adane, A., Mesnard, F., and Sauvageot, H. (2000). Modeling anomalous radar propagation using first-order two-state markov chains. pages 283–292.
- Haddad, B., Adane, A., Sauvageot, H., Sadouki, L., and Naili, R. (2004). Identification and filtering of rainfall and ground radar echoes using textural features. pages 4641–4656.
- Hedir, M., Demim, F., and Haddad, B. (2018). Radar echoes classification based on local descriptor. In *IEEE International Conference on Signal, Image, Vision and their Applications*, pages 1–6.
- Hedir, M., Demim, F., and Haddad, B. (2019). A comparative analysis of the ground clutter suppression on meteorological images. In *IEEE 6th International Conference on Image and Signal Processing and their Applications, Mostaganem, Algeria*, pages 1–7.
- Hedir, M. and Haddad, B. (2016). Automatic system for radar echoes filtering based on textural features and artificial intelligence.
- Islam, T., Rico-Ramirez, M., Han, D., and Srivastava, P. (2012). Artificial intelligence techniques for clutter identification with polarimetric radar signatures. pages 95–113.
- Kaissassou, S., Lenouo, A., Tchawoua, C., Lopez, P., and Gaye, A. (2015). Climatology of radar anomalous propagation over west africa. pages 1–12.
- Liu, F., Tang, Z., and Tang, J. (2013). Weber local binary pattern for local image description. pages 325–335.
- Malki, Z., Atlam, E., Hassanien, A., Dagneu, G., Elhosseini, M., and Gad, I. (2020). Association between weather data and covid-19 pandemic predicting mortality rate: Machine learning approaches. pages 110–137.
- Ojala, T., Pietikainen, M., and Maenpaa, T. (2002). Multiresolution grey-scale and rotation invariant texture classification with local binary patterns. pages 971–987.
- Paixao, E., Mirza, M., Shephard, M., Auld, H., Klaassen, J., and Smith, G. (2015). *An integrated approach for identifying homogeneous regions of extreme rainfall events and estimating IDF curves in Southern Ontario, Canada: Incorporating radar observations*.
- Rouigueb, A., Demim, F., Belaidi, H., Messaoui, A., Benatia, M., and Djamaa, B. (2023). Improving the license plate character segmentation using naïve bayesian network. In *Proceedings of the 20th International Conference on Informatics in Control, Automation and Robotics (ICINCO 2023), Rome, Italy*, pages 61–68. Giuseppina Gini; Henk Nijmeijer and Dimitar Filev.
- Rouigueb, A., Demim, F., Nemra, A., and Djamaa, B. (2022). Gearbox fault diagnosis using the short-time cepstral features. In *Proceedings of the 2nd IEEE International Conference on Advanced Electrical Engineering (ICAEE)*, pages 1–8. IEEE.